Description and Performance of the Fermilab FOCUS Spectrometer

Physicist 1 [a,1] Physicist 2 [b] Physicist 3 [c]

[a] *Fermi National Accelerator Laboratory, Batavia, IL 60510, USA*

[b] *Dip. di Fisica dell' Universita and INFN*

[c] *University of X*

Abstract

The magnetic spectrometer and charged and neutral particle identification sysetms used in experiment Fermilab E831 (FOCUS) are described in detail.

Key words: Spectrometer; Tracking detectors; Particle Identification; Monte-Carlo; Fermilab Tevatron

1 Introduction

FOCUS is a heavy quark photoproduction experiment located at the Wide Band Area of Fermilab. It is an upgraded version of its predecessor, E687 (1). The experiment collected data during the 1996-97 fixed target run at Fermilab, and is investigating several topics in charm physics including high precision studies of charm semileptonic decays, QCD studies using double charm events, a measurement of the absolute branching fraction for the D^0 meson, a systematic investigation of charm baryons and their lifetimes, and searches for D^0-$\overline{D^0}$ mixing, CP violation, rare and forbidden decays, and fully leptonic decays of the D^+. Based on experience with E687, FOCUS expects to fully reconstruct 10^6 charm particle decays.

[1] Present address:

2 Target Silicon Detector

As mentioned previously, the FOCUS experiment is an IMPROVED version of the previous FNAL photoproduction experiment E687[1]. One of the improvements made to the E687 detector is the installation of a new supplementary silicon vertex detector.

Four planes of silicon microstrip were installed in December 1996 and January 1997 during a month–long shutdown of the accelerator. As shown in Figure 1, these target silicon (TSSD or TS) planes were interleaved between the experimental target segments.

With the additional information from the TS detector utilized in the reconstruction software, we have significantly improved tracking resolution in the target region of the FOCUS spectrometer. We have increased lifetime resolution from about 50 fs to around 30 fs(see Figure 2); charm decays have a better signal/noise ratio with higher yields for the same significance of separation; and new techniques for particle reconstruction have been realized.

The target silicon information is present for roughly 2/3 of the FOCUS data and this information is included in the analysis of the FOCUS data.

Currently, additional software is being developed to reconstruct D meson *tracks* using the charm production vertex(see Figure **??**) and information from two target silicon planes.

The components of the Target Silicon consist of 4 planes of 25 micron pitch 300 micron thick planes of silicon microstrip detector and the electronics necessary to amplify, digitize and store the information from these planes of silicon.

Each silicon plane has 1024 channels, or about an inch of active area, which covers the majority of the photon beam size at the E831 target. The signals from the silicon are amplified by MSP1 preamplifiers recycled from Fermilab experiment E791.

After a 40 ft cable run, the pre–amplified signals are amplified again, then sampled and digitized with a 6 bit flash ADC in order to be stored in buffer memory. When the experimental trigger fires, two signals in the buffer memory, one *in–time* and one earlier sample, are fed into an arithmetic logic unit where the earlier sample is subtracted from the *in–time* sample, and a threshold comparison is performed. The sparsified data are given a channel address and then stored in another series of buffer memories until being stored on magnetic tape with the rest of the data comprising an E831 event (see Figures **??**).

The data, once collected, are available for analysis. In the present version

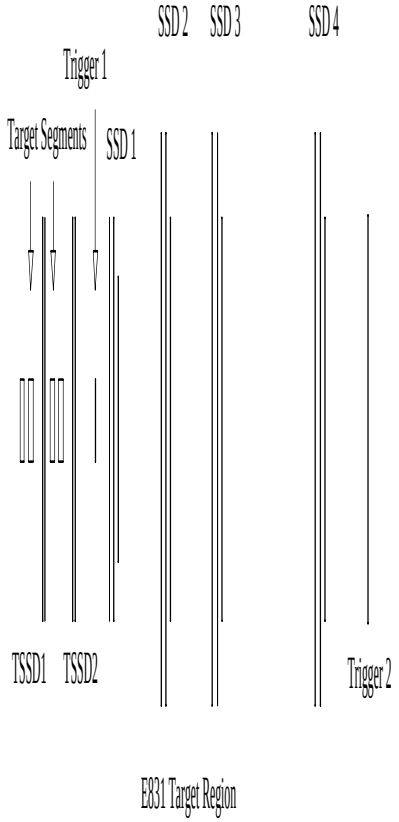

Fig. 1. Expanded view of the Target region configuration of the FOCUS spectrometer. The SSD's are the Milano silicon microvertex detector planes (re–used from E687), TSSD's are the Target silicon, there are 2 scintillator triggers (1 and 2), and 4 Beryllium Oxide targets. Note the TSSD plane doublets downstream and immediately upstream of the last target doublet. Using the additional information from these planes, we have improved lifetime resolution and increased the Signal to Noise of our charm decays. Additionally, the target segmentation allows us to reconstruct more charm decay vertices in air, thereby reducing contamination from hadrons interacting in the targets.

of the Target Silicon analysis code we project tracks reconstructed using the Milan SSD to target silicon planes and incorporate target silicon hits into the track fit. The refit tracks are then available for vertexing (see Figure 6).

3 PWC System

The multiwire proportional chamber (PWC) system for E831/FOCUS consisted of 20 signal planes grouped into 5 stations with 4 planes per station.

Fig. 2. Yield versus the Signal to Noise Ratio (S/N) from a non-optimized analysis using the same data of the decay mode $D^0 \rightarrow K^-\pi^+$. The analysis was done utilizing just the Milano Silicon (no TS) and a combination of the Milano and Target Silicon systems (New TS). Each point represents a different value of the statistical significance of the detachment (L/σ) of the $K^-\pi^+$ vertex from the primary interaction vertex. Notice the improvement in (S/N) as we increase (L/σ) from 5 to 14. An exponential fit to the fall off in yield indicates a proper time resolution of $\sim 49\ fs$ for the No TS analysis and $\sim 31\ fs$ for the new TS analysis. At the largest (L/σ), we have $\sim 50\%$ more yield and $\sim 40\%$ less background when we use the Target Silicon in the analysis.

These stations were labeled P0, P1, P2, P3 and P4, upstream to downstream. Stations P0, P1 and P2 were located between the two analysis magnets with P0 just down stream of M1. P3 was located just downstream of M2 and P4 was just downstream of the last Cerenkov counter C3.

There were two types of PWC stations, Type I (P0 and P3), and Type II (P1, P2 and P4).

Each station had four views. The X view wires ran vertically and measured horizontal position. The stereo angle for the U and V views was 11.3^o from the Y view. The orientation of the wires, which is the same for Type I and Type II, is shown in Fig. 7.

The Type I stations had an aperture of approximately 30 in. x 50 in. (larger

Fig. 3. Histograms of the mass distribution from a non-optimized analysis of the decay mode $D^+ \to K^-\pi^+\pi^+$. Decay candidates were selected (skim) if the reconstruction indicated that the D^+ *track* passed though one of the Target Silicon doublets. The D^+ *track* hypothesis was then tested using Target Silicon information, and if the hypothesis was confirmed, the candidate was selected for the second plot (perfect ts track). We retain 93% of the signal and remove 70% of the background by requiring confirmation of the D^+ *track* hypothesis using the Target Silicon information.

dimension is vertical)) with four anode views, YVUX in upstream to downstream order. The Type I anode and cathode planes consisted of copper-clad G-10 circuit boards laminated to solid G-10 frames milled for flatness. Wires were wound onto transfer frames, aligned and glued onto the frames and soldered to the circuit boards. Flexible ribbon cables were plugged into headers soldered onto the circuit boards and carried the anode signal to connectors located outside the gas volume. All cathode and anode planes in a station were stacked within a sealed aluminum gas box with Mylar windows and a removable cover plate for access. The planes were stacked onto precision machined locating pins that pass through two locating rings at one end of each plane. The locating pins fit into holes machined in the gas box and are visible from the outside so that survey and alignment of the planes may be easily accomplished without opening the gas box.

Type I anode wires were 0.8 mil diameter gold-plated tungsten under 65 gram equivalent tension. The wire spacing was 80 mils and the anode-cathode half-gap was 0.235 in. Cathode wires were 2.5 mil diameter Cu-Be and ran vertically with a pitch approximately 0.4 times that of the anodes. Because of their length, the X plane anode wires were glued to a support wire running

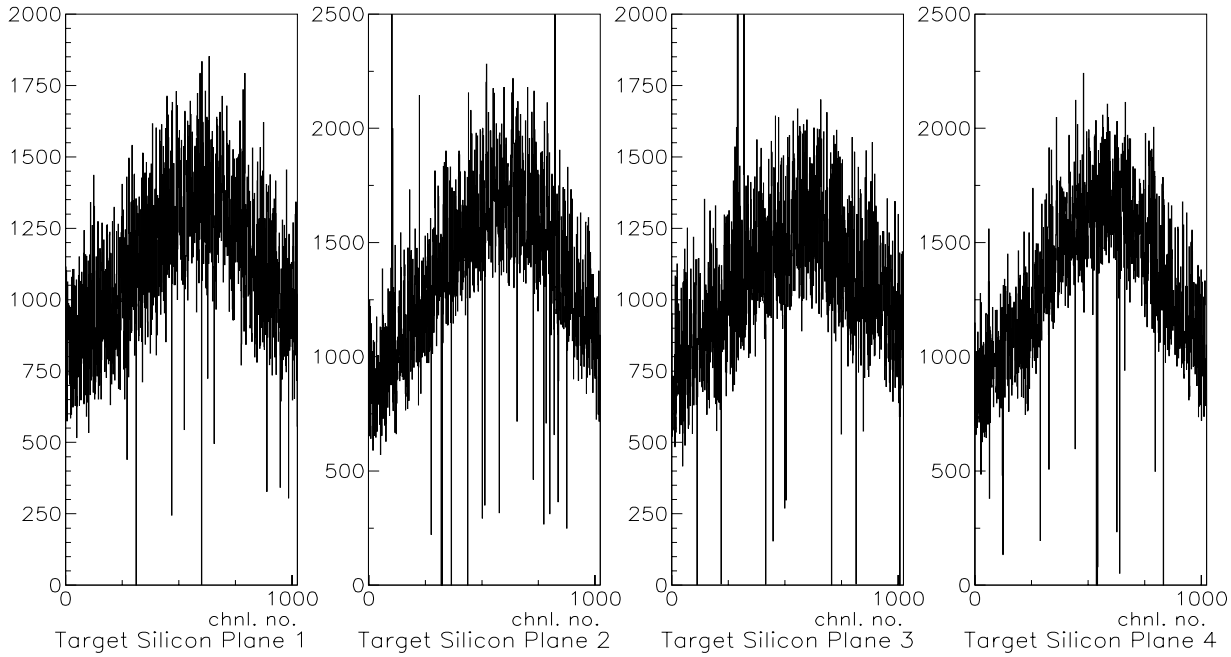

Fig. 4. Profile of hits in all for planes for a sample of photon data. The number of missing channels is on order of 1–2 %. Due to charge sharing, a missing channel does not necessarily translate to a loss in efficiency but rather a loss in resolution.

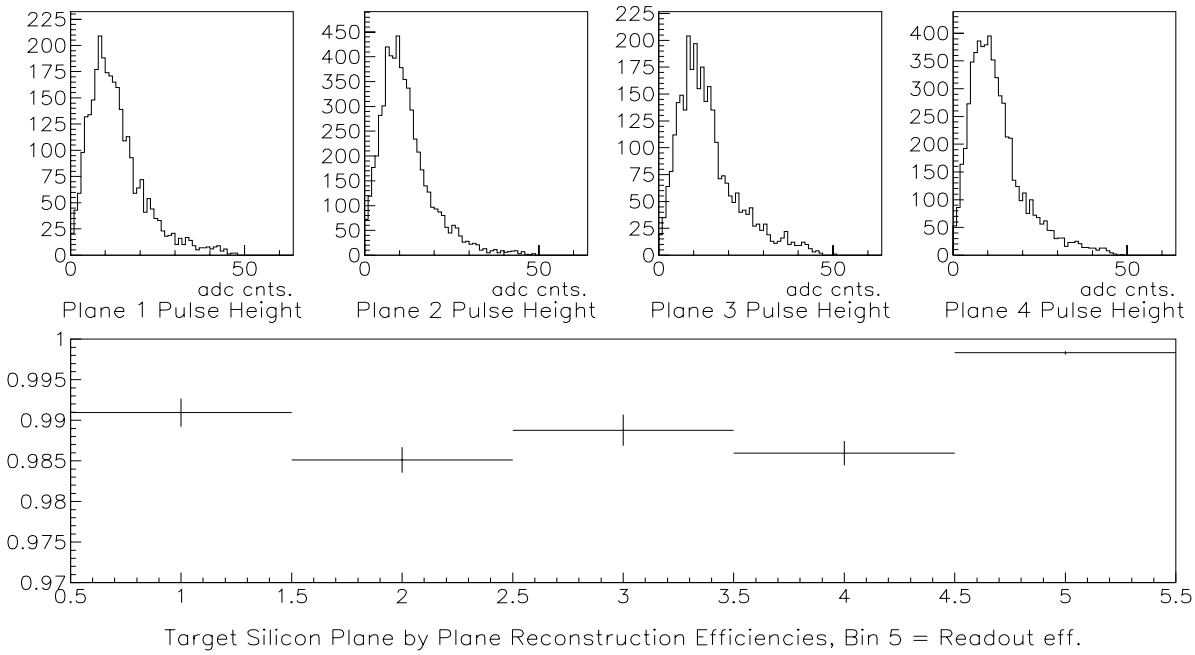

Fig. 5. Adc pulseheight for hits used to refit a track. A M.I.P. is clearly seen in all planes. The efficiency plane by plane is calculated for high momentum tracks on a run by run basis. We show these efficiencies in the lower plot. The fifth bin is an estimate of how often we must discard an event due to high multiplicity in a single plane and readout errors.

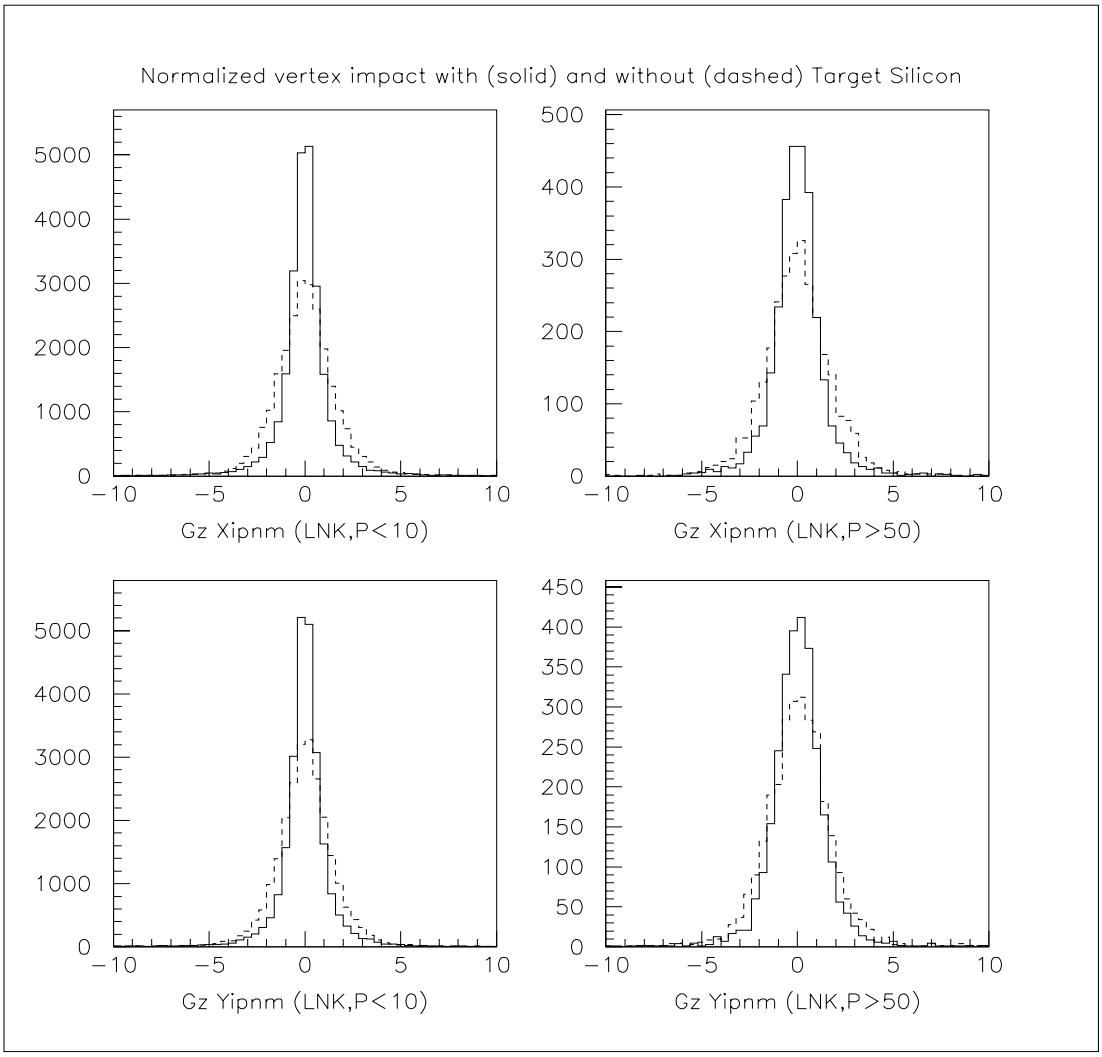

Fig. 6. Transverse normalized impact parameters. Tracks are projected back to a reconstructed vertex and normalized miss is computed. The dashed line represents the standard vertex reconstruction algorithm, the solid line is after including target silicon information into the fit(the error estimate is unchanged on purpose so that the increase in resolution is evident). Both low momentum ($P < 10\ GeV/c$) and high momentum ($P > 50\ GeV/c$) tracks are shown for both transverse (X and Y) projections.

horizontally across the middle of the plane in order to achieve electrostatic stability.

The numbers of instrumented wires for Type I stations were 376 for X plandes and 640 for Y, U and V planes giving a total of 2,296 wires each for P0 and P3.

The Type II stations P2, P2 and P4 had the same basic construction, number of views, stacking order and stereo angle but had a larger aperture of approximately 60 in. x 90 in. To provide extra stiffness, Type II planes had a layer

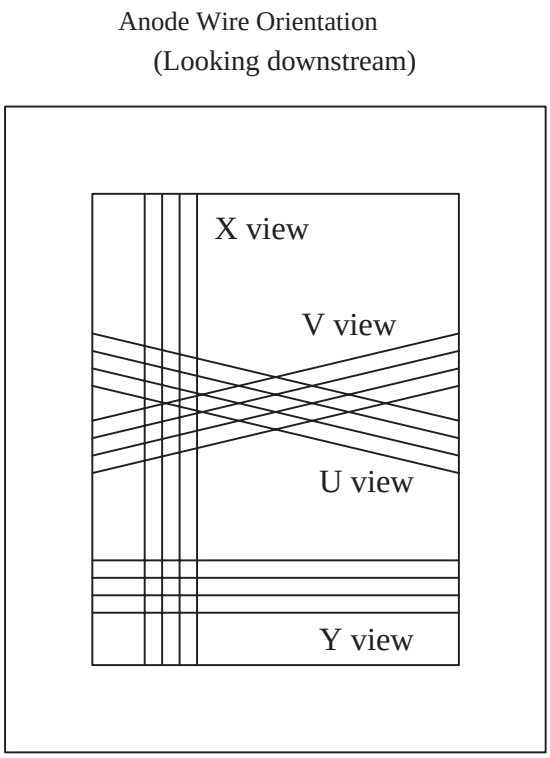

Fig. 7. Orientation of PWC wires

of stainless steel laminated within the frames.

The Type II anode planes used 1.0 mil gold-plated tungsten wire under 90 grams equivalent tension. The wire spacing was 130 mils and the half-gap was 0.240 in. The cathode wires were 3.5 mil Cu-Be and also ran vertically. Again the X view anode wires had to be supported, but here Mylar garlands running horizontally across the aperture were used to constrain the anode wires in plane between adjacent cathodes.

The numbers of instrumented wires for the Type II stations were 480 for X, 704 for Y and 768 for U and V planes, giving a total of 2,720 wires per Type station and thus a total of 12,752 instrument wires for the entire PWC system.

The gas mixture used was 65/35 Argon-Ethane and was bubbled through ethyl alcohol at 0° C before being distributed to the chamber system. Flow rates were approximately 0.5-1.0 SCFH for Type I stations and 1.0-2.0 SCFH for Type II stations, giving a complete gas exchange every 12-24 hours. A system of PhotoHelic sensors and solenoid valves at the input and output of each station was used to keep a nearly constant overpressure of 0.10-0.25 in. of water. Using this gas mixture , operating voltages of 3.30-3.60 kV for Type I planes and 2.80-3.20 kV for Type II planes produced good efficiency.

Signals from the anode wires were amplified and discriminated by preamplifiers mounted on the chambers. Low voltage power for the preamps was distributed via a system of 1/4 in. x 1 in. solid copper bus bars attached to the sides and bottom of the gas box. Small PC boards with edge connector sockets were mounted across the bus bars and the power connectors for the preamps plugged into these sockets.

Type I stations used 8 channel preamplifier cards with single-ended MECL II outputs, while the Type II stations used 16 channel (Nanometrics N341) preamps with complementary MECL 10K outputs. Both types of preamps were capable of detecting currents of less than $1\mu A$.

Discriminated signals from the preamps were sent to the counting room via 200ns to 350ns of delay cable, depending on station location, where they were received and reshaped before being sent to LeCroy ??? latches.

The latches were located in dedicated CAMAC crates, each containing a LeCroy ??? controller.

More readout details???

4 The Straw Tube System

Three straw tube wire chambers were used to cover the high pair flux region – a vertical stripe down the center of the spectrometer. Each chamber has three views, and within each view there are three nested straw layers.

All three chambers have a vertical (x measuring) view consisting of 30 straws (3 layers by 10 rows), and two angles views – $\pm 11.33^o$ from vertical. The most upstream chamber (ST0) is built with 138 cm long straws. Its angled views each consist of 114 straws (3 by 38). The other two chambers (ST1 and ST2) use 241 cm long straws and each angled view is comprised of 222 straws (3 by 74). (See figure 8.)

The views were built with 5 mm diameter straws. The straw material consists of two layers of $\sim 10\mu m$ thick mylar with a thin coating of copper on the inner surface. The anode wire is $20\mu m$ thick gold plated tungsten. In each straw, the wire is supported at both ends by a "v" grooved feedthrough and along the straw by a helicon support (2). The 241 cm straws have two helicon supports while the 114 cm straws require only one. The supports are placed as far from the center as possible to reduce the amount of scattering material in the highest flux region. The supports are necessary to keep the wire from snapping over to the ground surface on the inside of the tube. Each wire end is crimped, between a metal base with a HV pin connector and the plastic feedthrough, using a plastic collar (3). 60 grams of tension was applied to the wire during crimping, and typical resulting wire tensions are 45 to 50 grams.

The straws are operated with a slowly flowing gas mixture of 50% argon and 50% ethane, with a negligible positive pressure which is the result of flowing. The copper-coated straw wall is held at ground and the central wire is kept at a large positive voltage ($\sim$1600 volts).

The typical per-channel efficiency is 90%, with the largest source of inefficiency due to the small cord traversed by tracks at high radius.

When a track passes through a straw, the liberated electrons are collected on the wire. The resulting pulse is amplified and shaped by a preamp/discriminator card attached to the pins at the top end of each straw. The preamp card was designed by a group at Stanford for straws used in BNL experiment E781 (3). Each preamp card connects to six straw channels. The output of the preamp card is a differential ECL signal which is carried on twisted pair cables to redriver boards. The redriver boards regenerate pulses and extend all pulse widths to a minimum of 30 ns. This is done to prevent signal loss from attenuation in the 45 meter cable run between the redriver and the time to digital converter (TDC). The TDC assigns a rolling time stamp which is fixed when the experiment generates a trigger (common stop mode). LeCroy model 3377

TDC's with 1 ns timing resolution were used. The use of timing information exploits the electron drift time in the straw to improve resolution.

The primary use of the straws in FOCUS is to deterime track timing. Fermilab's Tevatron accelerator delivers beam in periodic buckets defined by the applied radio frequency (rf). Rf buckets are separated by $\sim 19ns$. The typical latched detector in FOCUS operates with a time window from 50 to 120 ns centered on the triggering bucket. Pair production in non-triggering buckets causes a sizable background in many detectors. Timing from the straws is used to determine the track's rf bucket in the following way. When a track passes through a straw view it has a 73% chance of creating a hit in each of the three layers. In two of the layers the charge will drift in one direction (let's say left) and in the third it will drift right. The sum of the average left drift time and the right drift time approximately equals the typical total drift time of 53 ns. Tracks from other rf buckets have sums which differ from 53 ns by multiples of the 19 ns bucket frequency. When available, timing information from several straw views can be combined to give a strong determination of a track's rf bucket. A typical distribution of left-right sums is shown in figure 9

5 The Outer E.M. Calorimeter

Photons and electrons are detected in the external region of the covered acceptance by the Outer Electromagnetic Calorimeter *OE*. The design for this detector provides full containment for e.m. showers and very fine longitudinal segmentation, namely 33 scintillator samplings organized in 9 longitudinal independent views, and a scintillator tiles tie-breaker located at shower maximum.

The OE calorimeter is located 900 cm from the target. Its external dimensions are $(255 \times 205)cm^2$, with an internal rectangular aperture $(51 \times 88)cm^2$. This corresponds to an angular acceptance for photons $(28 \leq |\theta_x| \leq 142)mrad$, $(49 \leq |\theta_y| \leq 114)mrad$. The OE calorimeter can be displaced both horizontally and vertically for calibration and access purposes. Counters are arranged in four independent quadrants in the X-Y plane (fig.1). A 3cm thick steel plate is installed upstream of M2 to shield the OE PMT's from the fringe magnetic field. The calorimeters are made of Pb (stiffened with a 6% Sb by weight) plates and scintillator layers (POPOP $C_{24}H_{12}N_2O_2$ doped with 8% naphtalene, and NE-102 were used). Scintillator layers are made of strips, whose light read-out is either individual (OE0, OE9 segments) or five-fold integrated by a light guide to a single PM (all other segments), see tab.1. Horizontal and vertical five-fold counters are interlaced as shown in fig.3.

5.1 Scintillating tile tie-breaker (s.b.)

mechanical structure, assembling procedure, etc

In tab.1 the detailed segmentation of the OE calorimeter is shown. Each counter in the calorimeter 1030??? is individually wrapped in $0.1\,mm$ Al foils and black plastic, was light-tightened and then assembled without liners in the mechanical structure, thus reducing dead regions. Counters are equipped with ten-stage, EMI-9902KB photomultiplier tubes (PMT) operating at a typical gain of 10^6 at $1000\,V$, with a quantum efficiency of 20% at $440\,nm$, which were individually tested in order to select only those with good linearity and small sensitivity to rate effect[EM1]. Gain vs high voltage supply was measured for all selected PMT's. PMT's are powered by LeCroy 1440 and custom-made FRAMM[EM2] HV systems, via a high-linearity, anode grounded voltage divider supplying $1.5\,mA$ at $1500\,V$. PMT's signals reach the counting room via coaxial cables, 60m long, where are converted by a Lecroy 1885????? Fastbus ADC using dual linear range technique: this means accepting input charges up to $200\,pC$ in the high resolution scale, and up to $1600\,pC$ in the coarser resolution scale ????replace???.

5.2 On-line Monitors

The calorimeter stability is controlled by monitoring the ADC's pedestals in both ranges during and between spills, and the HV supplies for the PMT's. Overall stability control for each channel is performed by a N_2 laser light source. ADC pedestals are acquired continuously in the interspills during data taking and cumulated in 1-2 hour periods. These pedestal runs are then analysed for changes with respect to the pedestal reference values, and all changes are recorded in a database for later use in data analysis. PMT's voltages are periodically read-back via computer, and discrepancies between setting and reading values $\geq 0.3\%$ are stored in database, while a warning condition is generated. The N_2 laser light is emitted at a wavelength of $330\,nm$. The light is converted by a $8\,mm$ wavelength shifter bar to a frequency equal to the frequency of the light emitted by the plastic scintillator used in the calorimeter. Quartz optical fibers (OPSICA SCF, Radiall Inc.) distributing the light to each PMT have a $200\,\mu m$ diameter core, a $400\,\mu m$ diameter silicon cladding, and a vynil protection. Each fiber is independently regulated in order to provide a signal corresponding to about 10 times the light emitted by one m.i.p. crossing one counter. In the case of a five-fold counter, this corresponds to about $\sim 10^4$ photons at the photocathode. The N_2 laser is constantly pulsed at a rate of $1\,Hz$. About $3 \div 4$ laser events are acquired during each interspill period: they get organised in 1-hour runs, and their statistical characteristics

stored in data bases. The Laser light output dependence on both the HV applied to the spark gap, and on the gas pressure in the cavity, were studied and optimised. An intrinsic stability for the laser output of $\pm 10\%$ was obtained. To improve this limit, two reference PMT's are used. Reference PMT's are kept at constant temperature, shielded from any beam effect and facing the same fiber bundle. By making use of the two reference PMT's the intrinsic stability of the gain monitor system was improved to $\pm 5\%$. Fig.4 shows a typical laser pulse height distribution, with and without the reference PMT's normalization algorithm. Similarly, fig.5 shows the effect of such normalization on the average dispersion of laser light pulses as seen by 660 counters in a dedicated run. Finally, fig.6.a) shows the response of a typical counter to the laser output during a standard 100-hour monitored DAQ period. The effect of laser and pedestal correction is shown in fig.6.b). The monitors installed are sensible to variations $\geq 1\%$.

5.3 The Response of the O.E. to mip's

Muons, pions and electrons have been used to determine the counters' geometry, to measure their light attenuation curves, to fine-equalise their gains and to calibrate the energy scale of the e.m. calorimeters. The counters' response to m.i.p.'s was studied in laboratory before assembling. HV's were set, in order to position the counters output for one m.i.p. at the suitable ADC channel, as shown in tab.2. This provides a dynamic range up to 25 GeV. The TM counters described in the Trigger Counters section provide a trigger signal for muons in the forward region $\sim \pm 40 mrad$: the OE movement allows to illuminate with muons also its outer region. A typical pulse distribution for one calorimeter's counter obtained from the muon trigger is shown in fig.7.a). The expected Landau distribution is here deteriorated by inclined muon tracks, sharing energy deposits between two counters. However, by locating the peak position we verify and, if necessary, adjust the PMT gain, reaching an approximate ($\pm 20\%$) equalization for all counters. After the equalization, profiles for all counters are determined by plotting their efficiencies, at a typical threshold of $0.3\, m.i.p.$, as a function of the track impact point measured by the MWPC (fig.8). By excluding tracks depositing more than 0.1 m.i.p. in the nearby counters, we get the energy distribution in fig.7.b), that can be fitted with the proper Landau curve.

A $30\, GeV$ pion beam was also used for the same purposes. Pencil-like, straight-through pions were selected by a three-counter coincidence system located upstream and downstream the OE ($1 \times 1\, cm^2, \pm 4\, mrad$ max divergence), while pions interacting in the calorimeter were rejected using anticoincidence counters. Simulations show that hadronic showers are suppressed by this setup-up better than a factor 10^2????. No differences have been found between energy

deposits obtained with either muon tracks (selected to avoid geometry effects) or straight-through pion beam calibration procedures, as shown in fig.7.c). Finally, fig.9 shows typical attenuation curves for counters with different lengths and widths. By following the described procedure, peaks of Landau distributions are used to intercalibrate the counters, and to fit their attenuation curves.

5.4 Run-dependent corrections to energy calibration via monitoring of E/P and π^0 peaks (s.b.), and γe^+e^- (h.m.)

5.5 Energy calibration, Resolution and Performances

The energy range for photons and electrons in the calorimeters' acceptances was studied using a photon-gluon fusion, Lund fragmentation based Monte Carlo program[EM3], which predicts typical photon energies for the OE in the range 1-10GeV, while electron energies in charm semileptonic decays are up to 30GeV.

The response of the calorimeters to photon- and electron-initiated e.m. showers, their linearity, the scale factor between detected energy and incident energy, and their energy resolutions have been studied using a GEANT simulation. In figure xxxx we see a GEANT simulation of a shower initiated by a x GeV electron.

The detected energy is parametrised as

$$E_{detect} = \frac{E}{\alpha} \pm \frac{\sigma_{FWHM}}{\sqrt{E\,[GeV]}}. \qquad (i.1)$$

where E is the particle incident energy, E_{detect} is the particle energy deposit in the calorimeters active layers, and $\sigma_{FWHM} \equiv FWHM/2.36$ is the relative energy resolution at $E = 1GeV$.

For the OE $\alpha_{MC} = 5.58 \pm 0.02$ when computed at $E = 10\,GeV$. The variation of α_{MC} is $\pm 5\%$ in the range $E = 1 \div 6GeV$ and only $\pm 2\%$ for $E \geq 6\,GeV$, while an energy resolution $\sigma_{FWHM} = 13\%$ is expected.

The energy scale and resolution as predicted by Monte Carlo have been verified using physical signals. Broad band electrons in the momentum range 10-20GeV were also used for the energy calibration, finding results in overall agreement. The OE response to a primary beam of nominally 18GeV electrons, with a momentum spread $\sim 30\%$, is shown in fig.IV.E.2: electron deposits are clearly

visible, along with contaminating m.i.p.'s and showering hadrons.

Invariant mass peaks of π^0, D^{*0} (fig.IV.E.1.a,b) were used to fine-tune the energy scale. Optimization of the peak positions provides $\alpha_{OE} = 5.87 \pm 0.13$, while the experimental width observed is compatible with $\sigma_{FWHM} = 15\%$, in agreement with the resolution predicted by the simulation.

5.6 Reconstruction of neutral showers (a.r.)

procedure, algorithm, role of tiles, tiles efficiencies, reconstruction efficiencies for showers, as a function of shower energy and impact point. Space resolution using electrons reconstructed as showers

this is the old text: The reconstruction algorithm begins with the identification of clustered energy deposits. Clusters of energy deposits associated with the projection of charged tracks reconstructed in the magnetic spectrometer are tagged. The reconstruction of neutral showers uses the remaining clusters.

Energy deposits (in ADC counts units) for each counter are multiplied by the calibration constants, corrected for light attenuation in the counters, and then summed up to determine the detected energy associated to each cluster.

Pairs of clusters in the two orthogonal X-Y views of each OE segment are formed using energy balance as criterium. Neutral showers are formed by aligned X-Y pairs in the different OE segments. The diagonal counters and the tiles are used to resolve ambiguities.

The coordinates of shower centroids are determined considering the energy deposit in each counter of the X-Y pairs. Once corrected for systematic effects, shower centroids determine the incidence point of photons. The typical resolution on the shower point of incidence, as measured by the sampling at shower maximum is of $\pm 0.9cm$ at 3GeV and $\pm 0.3cm$ at 10GeV.

Finally, the sum of energy clusters longitudinally forming a reconstructed photon track enters the (i.1) as the detected energy term.

The reconstruction efficiency for single isolated showers was measured using primary Bethe-Heitler e+e- pairs. The e+e- tracks found in the proportional chambers were projected onto the OE front. Shower reconstruction was then performed using all available clusters. The efficiency for reconstructing the shower associated to the e+ or e- track was greater than 95%, over the range 2-14 GeV/c^2.

5.7 electron identification

The OE calorimeters extends significantly the $e - \pi$ rejection, beyond the Cerenkov momentum range, from 6 to 25 GeV and from 17 to 90 GeV, respectively.

To optimize the algorithms for the electron identification, we used e+e- primary Bethe-Heitler pairs and e+e- Bethe-Heitler pairs from photon conversions in hadronic events, making use of the E687 magnetic spectrometer to measure their momenta ($\Delta P/P \leq 0.5\%$ in the momentum range of interest). To reproduce standard experimental conditions, the analysis magnets are set to the currents used during normal data taking. The correlation between the energy deposit in the calorimeter and the electron momentum measured by the spectrometer is shown in fig.IV.E.3.

The identification algorithms have been developed in the framework of the Discriminant Analysis[EM4], which allows to efficiently distinguish between two or more groups of events, once a set of meaningful variables (called "Discriminant Variables") is found, which provides good discrimination for cases with known group membership. As members of the known groups we used muons, beam pions, pions from K_S^0 decay, and e+e- pairs. The patterns of energy deposits, and the ratio E/P_{PWC} between the energy measured by the calorimeters and the track momentum as measured by the magnetic spectrometer were used as discriminant variables (Tab.IV.E.I). The overall hadron rejection obtained for an 85% electron efficiency is $\sim 1 \cdot 10^{-2}$. Fig.IV.E.5 shows the behaviour of the efficiency for electrons and the rejection for hadrons as a function of the track momentum.

5.8 results on physical signals (s.b.+a.r.)

eta, D, Kpipi0, semielectronics, ????* Fig.IV.E.6. shows the $\bar{K}^{*0}$ invariant mass peak from the semileptonic decay $D^{*+} \to \bar{K}^{*0}\, e^+\, \nu_e$, where the electron is identified by the e.m. calorimeter.

Add muon id via OE

S. Bianco *et al.*, INFN-Frascati note LNF-85/49(R).

G. Bologna *et al.*, Nucl. Instr. and Meth. **192** (1982) 315.

M. Enorini *et al.*, INFN-Frascati note LNF-84/22(R).

Various Authors, Statistical Package for the Social Scienses (SPSS), McGraw-

Hill, New York (1975).

6 Inner Electromagnetic Calorimeter

The Inner Electromagnetic calorimeter (IE) is composed of lead glass blocks arranged in a tower geometry. There are two sides to the detector with a central gap to allow the passage of the intense beam of non-interacting photons and converted e^+e^- pairs. A schematic drawing of the layout of the detector is shown in Figure 10.

6.1 Description of individual lead glass blocks

The blocks were cast by Schott and are of type F-2 with a radiation length of X_0=3.21cm. Glass of type F-2 is composed of roughly 45% silica, 45% lead oxide, 5% sodium oxide, and 5% potassium oxide. Each block has dimensions 5.8 cm×5.8 cm×60.2cm. and hence, is 18.75 X_0 and 2.2 interaction lengths.

The phototube end of the glass block was prepared such that a phototube could easily be replaced. A glass disk with a diameter of 2.151 inches and a thickness of 0.250 inches was glued onto the center of each lead glass block using Epotek 301 optical grade epoxy. A magnetic shield and a phenolic block (for support) were both glued to the block and disk using 3M–2216 epoxy. The blocks were wrapped with 0.0005 inch thick aluminized mylar with the aluminum side placed next to the glass. Each block was individually measured in both transverse dimensions.

The photomultiplier tubes are of type Amperex XP2202 FL/B. The "FL" stands for flying leads. The tubes are 10 stage with a bialkali photocathode. The tubes have a maximum external diameter of 51.5 mm and an active photocathode area sensitivity of 44 mm. The voltage on the base is typically -1200V with an average gain of 1.2×10^5. The phototubes are fitted with a layer of optical gel, a mixture (by volume) of approximately 1.0:2.0:0.3 of GE RTV615A, GE SF96-50 silicone fluid, and GE RTV615B curing agent. A Wratten 2A filter is embedded in the gel to reduce the sensitivity to variations in shower depth. The gel was chosen to be extremely soft in order to make good optical contact with the lead glass. Optical contact between the block and phototube is thus provided by the silicone gel with an index of refraction of 1.45, which is between that of the glass (1.6) and the phototube face (1.4).

6.2 Description of the Lead Glass Array

The FOCUS IE consists of 802 blocks of Schott F-2 lead glass (radiation length X_0=3.21 cm.) The layout is 37 blocks high by 22 blocks wide. A 5.5 inch gap exists between the 11th and 12th column of blocks to allow the pairs to pass. Between the 11th and 12th columns there are two 1/4 inch steel plates that were inserted for rigidity and a 5 inch air gap. The outside dimensions are 55.74 inches wide by 84.5 inches high. The air gap has two aluminum I-beams that keep the steel plates from deforming. At the downstream edge of the gap there are located three lead bricks. The bricks are 2 inches high by 5 inches wide by 8 inches long. They were located inside the calorimeter frame to eliminate any holes in the pair shield and the Beam Gamma Counter in front of the hadron calorimeter.

The arrangement of blocks can be seen in Figure 10. In addition, the arrangement of the summing boards described in Section 6.6 can be seen.

The dimensions of each block were separately measured and their positions within the array were chosen to minimize cracks. This process was very important as roughly 10% of the blocks were slightly smaller than the rest. Cracks were further minimized by two tightening rods per row that pushed the blocks close together.

In order to protect the phototubes, the entire array was housed in a light tight box. (See Figure 11.) Ventilation was supplied to keep the temperature inside the box below 40.

6.3 Readout

Readout was accomplished using 16 Lecroy 1881M ADC modules. Each module supplies 64 channels of 13-bit ADC readout. The gate time was 120 ns. The triggering and readout method is described in the DAQ section.

6.4 Calibration system and method

Initial energy calibrations for each block were roughly determined using the Čerenkov light from halo muons and refined using an iterative π^0 reconstruction process. In order to track time dependent changes in phototube gains and block opacity, a flasher system was employed.

A xenon flash tube was flashed several times during each inter-spill and pulse

heights were recorded for each of the 802 phototubes as well as several reference tubes. Light was distributed to the front of each lead glass block by a fiber optic distribution system.

By comparing the time dependence of the flasher response with the response of the reference tubes, the IE array calibration was kept relatively constant. This calibration was cross-checked and corrected by reconstructing π^0s at various times in the run.

6.5 Performance

6.6 Dielectron trigger

In order to form a fast trigger based on energy in the inner electromagnetic calorimeter, dedicated summing boards were used. These boards provided pass-throughs for the signals from individual lead glass blocks. They also provided amplified outputs for the sum of pulse heights from groups of 9 blocks. All channels in the IE were arranged into groups of 9, roughly based on E_T for the purpose of providing trigger inputs.

The dilectron busline was specifically designed to trigger on the decay $J/\psi \rightarrow e^+e^-$. Using the summed outputs, sums were made of six regions of the IE (three roughly square regions on each side of the detector). The trigger required greater than xx GeV deposited in two non-adjacent regions. Regions seperated by the pair gap are considered non-adjacent. Custom built electronics provided the 6 energy sums. The trigger busline was formed using LeCroy xxxx discriminators and a LeCroy xxxx PLU and finally sent to the counting room.

7 Hadron Calorimeter

The FOCUS photoproduction experiment required a hadron calorimeter for triggering on events with hadronic final states to enhance these relative to the more abundant e^+e^- conversions of the photons. The HC had to be fast enough to be included in the first level trigger and to be large enough to cover the desired solid angle (approximately 100 mrad). With these primary goals in mind we constructed a hadron calorimeter with the design objectives of providing good hadron energy resolution, good position resolution and hadronic shower recognition capability. The FOCUS (E831) predecessor, the E687 experiment(4), used a sampling gas hadron calorimeter with tower

readout geometry(5). Iron plates were interspersed with planes of extruded aluminum proportional tubes. Capacitively induced signals on electrode pads with a cylindrical geometry were read out. The E687 HC was used in the second level trigger. In constructing the E831 hadron calorimeter to meet the experiment requirements, we used the E687 HC iron structure and we replaced the proportional tube planes with scintillating tile planes using fiber readout in a tower geometry. The scintillator has a fast response which is important for inclusion into the first level trigger and also the signal suffers from less noise giving more powerful rejection of non-hadronic background. A schematic view of the calorimeter is shown in Fig. 12.

The FOCUS hadron calorimeter consists of 28 305x208x4.4 cm^3 iron absorber plates[2] interspersed with 0.7 cm thick scintillator planes (Kuraray SCSN-81 polystyrene) as the sensitive material for a total of 7.8 interaction lengths and 72.7 radiation lengths. The layers comprising each active plane of the calorimeter are shown in Fig. 13. The active planes were encased in an aluminum frame to ensure mechanical stability. Each plane was formed by 66 tiles of different size: 20x20 cm^2 in the central region and either 40x40 cm^2 or 50x50 cm^2 in the outer region (Fig. 12). One of the HC tiles is shown in Fig. 14. Each tile was painted on the 0.7 cm thick side edge with white reflective paint to avoid light leakage to the neighbouring tiles, while the front and rear surfaces were covered with a white Tyvek plastic sheet (0.014 cm). One of the 2 Tyvek layers was then followed by a polystyrene coverplate (0.317 cm), while the second was attached to a PVC plane (0.600 cm). A steel skin (0.15 cm) was then applied to the polystyrene coverplate.

The blue scintillation light of the tiles was converted into green light by wave length shifting (WLS) plastic fibers (Kuraray Y11, 0.89 mm diameter). To increase light output, two fibers were used, laid one on top of the other in an alpha shaped groove machined in the scintillator tile(6) (Fig. 14). The WLS fibers had an attenuation length of about 3 m. In order to improve light transmission and to avoid having active WLS fibers outside of the tiles, clear plastic fibers with double cladding (attenuation length of 7 m) were used from just outside each tile to the phototube. The connection between the four WLS fiber ends of each tile and the clear fibers was made by splicing them thermally(7). The light loss due to the splicing was typically 10%. These four fibers ran outside each tile and went into a connector fixed in the aluminum frame. In order to equalize the time of arrival of the light to the phototubes, the clear fibers were of equal lengths for all tiles and had to be routed in winding grooves cut in the white PVC plastic covering (Fig. 13). A readout fiber connected to an EMI 9902 KB photomultiplier tube (non green-extended) was inserted in another connector which mated with that in the aluminum frame. The readout fibers were not connected directly to the photomultiplier

[2] The first 2 planes were 6.4 cm and 5.1 cm thick respectively.

tubes (PMTs), but interfaced with a square mixing block. This ensured that the light from each fiber uniformly illuminated the PMT photocathode(8).

The 28 HC planes were grouped together in 3 sections. The first upstream 9 planes made up the first section, the second 15 planes the second section and the third section consisted of the last 4 planes. Fibers from tiles occupying the same x and y position of the same section were grouped together and connected to the same phototube to give a *tower*. With 66 towers per section there were 198 readout channels.

Even though the phototubes were non green-extended, the tile response to a minimum ionizing particle (MIP) was acceptable. The results of a test performed with cosmic rays showed that the average photoelectron yield was about 3 photo-electrons (p.e.) per MIP for the 50x50 cm^2 tile and about 5 p.e. per MIP for the 20x20 cm^2 tile.

7.1 Electronics

The phototube anode signals were sent to ADCs while the dynode signals were sent to the trigger electronics.

7.1.1 HC electronics

The 198 PMT anode signals were sent directly to 4 Lecroy 1881M Fastbus ADCs. The outputs were then sent to the Data Acquisition through a Lecroy 9101 Fastbus Smart Crate Controller (FSCC). Each ADC module contained 64 channels of analog-to-digital converter (ADC) with current integrating inputs, a 13-bit resolution, a high sensitivity of 50 fC/count and a short conversion time of 12μsec. The integration time was set to 100 ns. The 1881M contained a multiple event buffer which could store up to 64 events. The FSCC allowed readout and recording of the 198 HC channels.

7.1.2 HC trigger electronics

The 198 PMT dynode outputs were sent to 15 CAMAC summer cards. These cards were custom designed and built by the Fermilab Physics Section Electrical Engineering Group. Each card had 16 input channels and 2 different outputs. Weights/gains could be set for each input channel and for each of the 2 outputs separately. One output was used for the energy sum and the second for the transverse energy sum. The weights could be in the range of approximately -0.95 to + 0.95. Negative weights inverted the signal. Delay from input to output was about 6.5 ns.

An integrator module, built by the Fermilab Physics Section Electrical Engineering Group, took as input, from the summer card that gave the sum of the 198 HC channels, the final analog sum. A copy of the input was sent to each of the four different integrators that were continuously integrating and clearing. The module therefore did not need a gate but ran off either an external clock signal (the accelerator RF) or an internal 50 MHz clock (for tests). Each integrator integrated for 2 clock cycles and took two clock cycles to clear before starting to integrate again. Each integrator started one clock cycle after the previous one so that it overlapped by one clock cycle and there were always two integrators operating at any time. When any of the four integrators saw a signal above its CAMAC settable threshold it produced an output width of at least one clock cycle. The trailing edge was fixed with respect to the clock but the leading edge depended on when the integral exceeded the threshold. Each of the 4 integrators had its own threshold, so that each could be individually correctly calibrated. Delay from input to output was about 6 ns in additional to the integration time required to reach the desired threshold.
This integrator generated the hadronic energy trigger, i.e. a NIM signal, when the hadronic trigger was above a certain threshold. The output signal from this module was then sent to a Programmable Gate Generator, in the Electronics Room upstairs from the experimental hall, to give our First Level Trigger (FLT).

Taking into account all time delays a trigger signal was available for FLT processing around 0.34 μs after an interaction in the experiment target.

7.2 Monitoring systems

Two monitoring systems were implemented: a ^{60}Co source that could illuminate every tile and check its status and its corresponding phototube, and a laser system to monitor phototube gain.

One system consisted of a thin steel wire with a small ^{60}Co source embedded in its tip. This wire could be unrolled from a supporting cylinder and driven by a step motor into thin metal tubes that went through the aluminum frames. In order to illuminate each tile, each active plane was provided with 8 metal tubes. The system gave a measure of the detection efficiency of both the tile and the corresponding phototube.(9).

The laser system consisted of a UV laser illuminating a piece of scintillator made of the same plastic scintillator as the one used in the active planes. The light was optically diffused by a lucite cone and transmitted by 198 glass fibers to 4 different boxes in which they illuminated plastic WLS fibers of the same type as used in the calorimeter tiles. The WLS fibers were then routed

to the 198 calorimeter phototubes. To calculate the signal ratio (calorimeter phototube)/(reference phototubes), two fibers were also routed to a pair of reference phototubes, which were maintained at constant temperature. These two signals were sent to one of the 4 1881M Fastbus ADCs described above to allow recording of these signals. The system was used to check the gain stability of the 198 phototubes.

7.3 Calorimeter calibration and performance

Calibrations of the calorimeter and gain balancing were performed with muons and pions.

To equalize the response of each tile to a MIP, a muon beam was directed towards the HC. In Fig. 15, typical muon pulse height spectra, in ADC counts above pedestal, for a tower in section 1, 2 and 3 are shown. The fit of the distributions was performed with a Landau function plus a negative exponential. The voltages of the phototubes were changed at the beginning of the run to obtain the gain balancing shown in Fig. 16; vertical lines represent the sigmas of the Landau functions. The ratios of the ADC counts corresponding to the muon peak of a tower in sections 1, 2 and 3 were set approximately to 10:16.5:6 (see horizontal lines in Fig. 16). The values were chosen to be close to the ratio of numbers of layers (9:15:4), and as a compromise between getting a high dynamic range up to $\simeq$ 60 GeV, needed in section 1 and 2, and a good separation between muon peaks and background, needed in section 3. During the year of data taking the gain balancing was checked with muon beams and source calibrations. We had to change the phototube voltages twice during the entire run, due to a shift towards lower gains as monitored by the response to muon beams.

The calibration for hadronic showers was performed twice during the data taking period with a pion beam, ranging approximately from 25 GeV/c to 75 GeV/c in momentum, directed toward a single tile region ($\simeq$ 20 x 20 cm^2 region). The resolution curve and the linearity plot as a function of the pion momentum are shown in Fig. 17. The calorimeter provided a linear response in the momentum range considered and a reasonable resolution ($\sigma_E/E = 85\%/\sqrt{E} + 0.86\%$) given the non-compensating nature of the calorimeter. This resolution is well reproduced by a GEANT based Monte Carlo (Fig. 17). This was a significant improvement in resolution over the E687 HC ($\sigma_E/E = 132.6\%/\sqrt{E}$).

7.3.1 Hadronic trigger

As previously described, the HC phototube dynode signals were sent to trigger summer cards and to an integrator card containing 4 integrators with a gate of 2 RF buckets ($\simeq$ 38 ns). If the total HC energy was greater than about 20 GeV then the hadronic trigger, included in the first level trigger was set. The trigger efficiency versus the total energy, given by the sum of all 198 ADCs, is shown in Fig. 18. For a primary beam of 4x10^{12} protons/spill, the 10 MHz rate, due mostly to photon conversions, was reduced to about 300 kHz with the use of scintillator hodoscopes. With the addition of the hadronic trigger, the first level trigger rate was reduced further to about 3 kHz, corresponding to a 1% deadtime.

7.4 Conclusions for the HC

The FOCUS (E831) hadron calorimeter was successfully used in the 1996-97 Fermilab fixed target data taking run. It was included in the first level trigger and proved to be fast and efficient. Off-line reconstruction programs have been developed in order to allow the use of the calorimeter in physics analysis including neutral hadrons. In particular, energy and position of the hadronic showers are made available to allow the reconstruction of charmed hadrons decays into charged and neutral hadrons (neutrons and K^0_L). In the predecessor experiment, E687, the HC had already been used to reconstruct the decay $\Sigma^{\pm} \rightarrow n\pi^{\pm}$(10; 11; 12; 13) for the detection of the 3 charmed baryons Λ^+_c (10), Ω^o_c (11) and Ξ^+_c(13).

8 Cherenkov Particle Identification

```
CITADL NIM Outline
Motivation & background
a  LOGIC method and its shortcomings
>ISTAT code
>PEOFF & SIGPE cuts
>Light particle bias.
>Noise suseptability
>>Acc versus xcell

b. Increased flexibility from a  likelihood based algorithm
>>Important for Cabibbo suppressed decays
>>Ability to incorporate noise
>Avoid arbitrary cuts
```

Basic algorithm
a Motivation for discrete versus continuous likelihood
>Hard to model ph dist due to noise
>Less calib since insensitive tu gain fluctuations
>Many cells result in a nearly
continuous kaonicity anyway

b Poisson firing probabilities
Incorporating noise & Pileup
De Morgan Law

c. CITADL CL?

Implementation
>Light sharing
>Scaler method for instantaneous intensity
>CITADL CL speedups
>data base management?

Calibration methods
a. Hardware Calibration
>Gain balancing with pulsers
>Pedistal suppression

b. Ks likelihood parabolas
>Baraometer plot
c. Accid versus NPE and run period selection.
d. geometry
e. PH cut point
>Intrinsic and extrinsic noise
>Poisson mean acc vrs Npe

Run dependence from Oddpack
>Barometer plots
>Ks , lambda, and phi mis-id versus run
>>sideband technique

Performance
>Weatherman plots for central and peripheral cells
>Integrated kaonicity and pionicity for D Lamba Ks
>Kpipi ref into KKpi versus
kaonicity

```
>KK and pipi FOCUS vrs E687
>Golden mode cut trees?
```

..

References

[1] E687 Collaboration, P.L. Frabetti et al., *Nucl. Instrum. Meth.* **A320** (1992) 519.

[2] S. H. Oh and A. T. Goshaw and W. J. Robertson, *Nucl. Instrum. Me th.* **A309** (1991) 368.

[3] S. Graessle et al., *Nucl. Instrum. Me th.* **A367** (1995) 138.

[4] P. L. Frabetti et al., Nuclear Instruments and Methods A 320 (1992) 519.

[5] S. Park et al., Nuclear Instruments and Methods A 289 (1990) 496.

[6] V. Arena et al., Tile Fiber Calorimeter, in:World Scientific, *Proceedings SCIFI '93, workshop on Scintillating Fiber Detectors* (Notre Dame, Indiana-USA,1993) 24-28.

[7] G. Apollinari, D. Scepanovic and S. White, Nuclear Instruments and Methods A 311 (1992).

[8] E.C. Dukes and J. White, Monte Carlo Results on the Design of Light Guides for Scintillating Fiber Calorimeters, in: World Scientific, *Proceedings First International Conference on Calorimetry in High Energy Physics* (eds. D.F. Anderson, M. Derrick, H.E. Fisk, A. Para and C.M. Sazama, Batavia, IL, 1990) 177-188.

[9] V. Barnes et al., Calibration of Scintillating Calorimeters,in: World Scientific, *Proceedings First International Conference on Calorimetry in High Energy Physics* (eds. D.F. Anderson, M. Derrick, H.E. Fisk, A. Para and C.M. Sazama, Batavia, IL, 1990) 189-195.

[10] P. L. Frabetti et al., Phys. Lett. B 328 (1994) 193.

[11] P. L. Frabetti et al., Phys. Lett. B 338 (1994) 106.

[12] V. Arena et al., Nuclear Instruments and Methods A 374 (1996) 359.

[13] P. L. Frabetti et al., Phys. Lett. B 427 (1998) 211.

A APPENDIX

Here is the appendix.

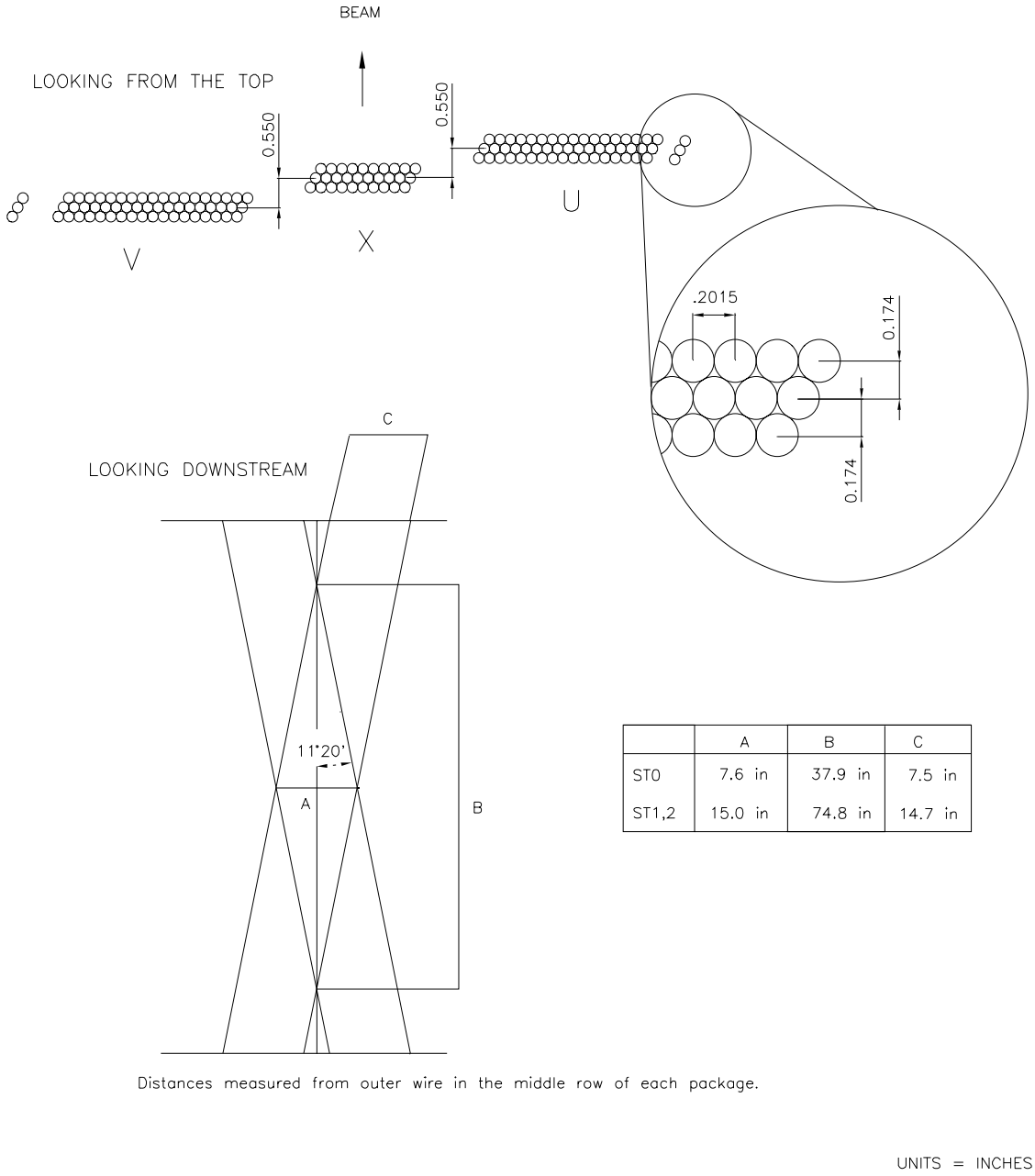

	A	B	C
ST0	7.6 in	37.9 in	7.5 in
ST1,2	15.0 in	74.8 in	14.7 in

Fig. 8. Schematic of the straw tube detectors showing basic layout and dimensions.

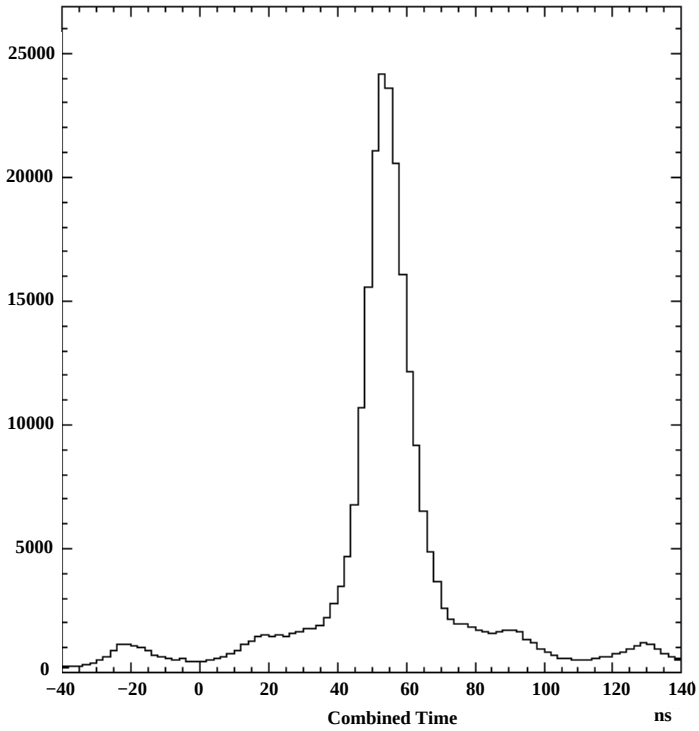

Fig. 9. This plot shows the sum of left and right drift times for straw hit triplets. The large peak is from the triggering rf bucket, and the smaller peaks are from tracks in other buckets.

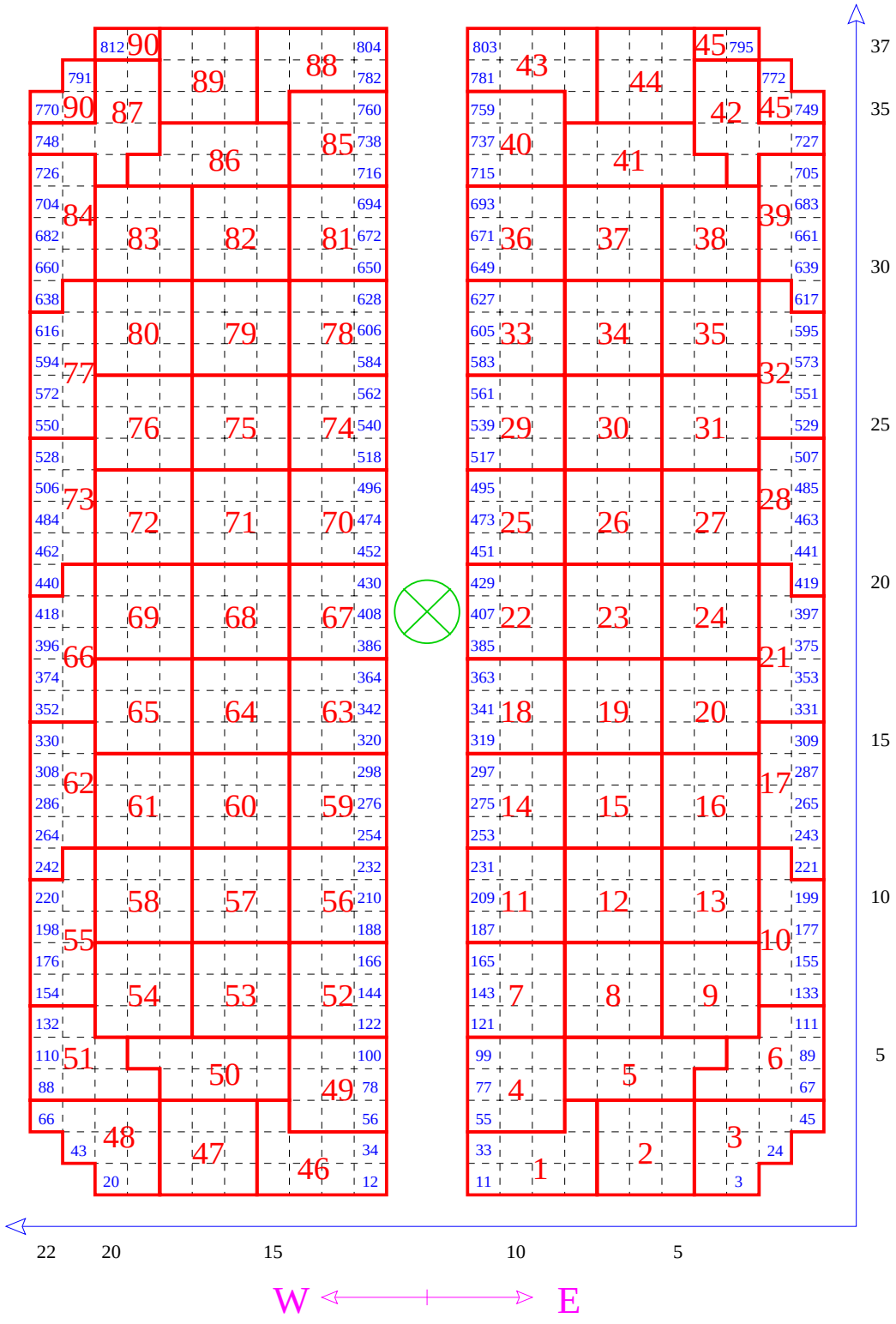

Fig. 10. Schematic of IE block arrangement. Blocks are shown with small numbers and dashed lines; arrangement of summing boards are shown with thick lines and large numbers

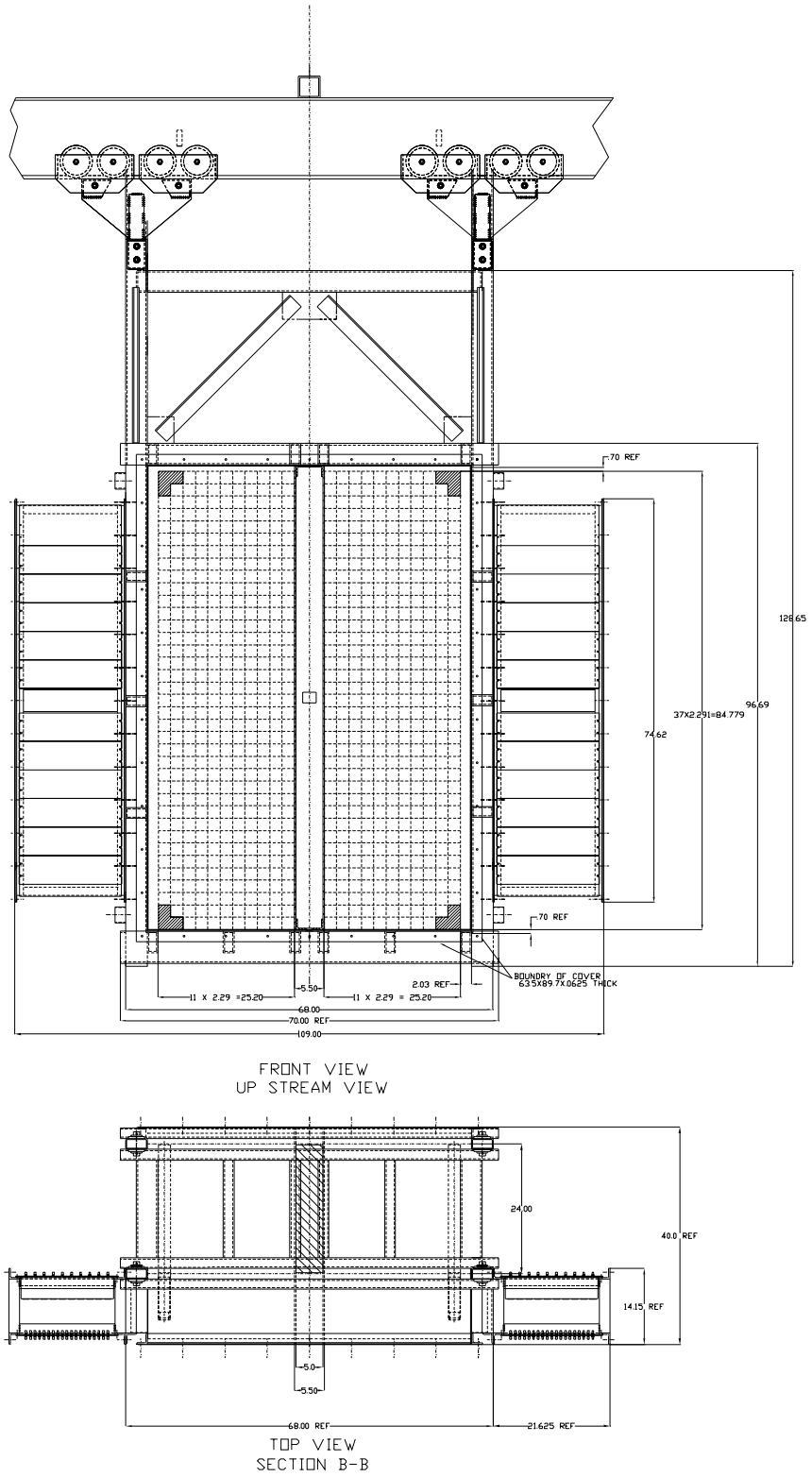

Fig. 11. Layout of the IE detector and support frame

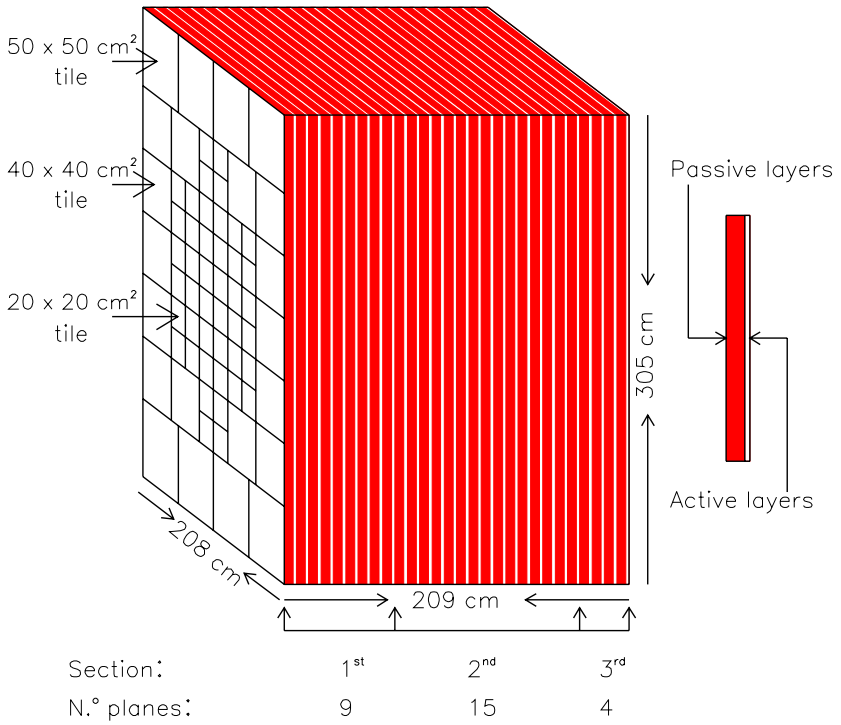

Fig. 12. Hadron Calorimeter schematic view

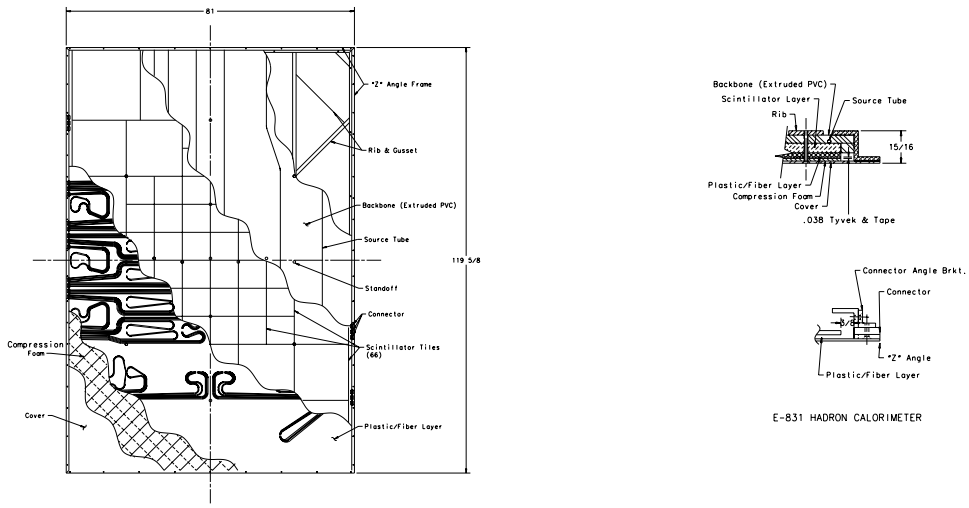

Fig. 13. Layers compounding each active plane of the calorimeter.

Fig. 14. Picture of one of the HC tiles.

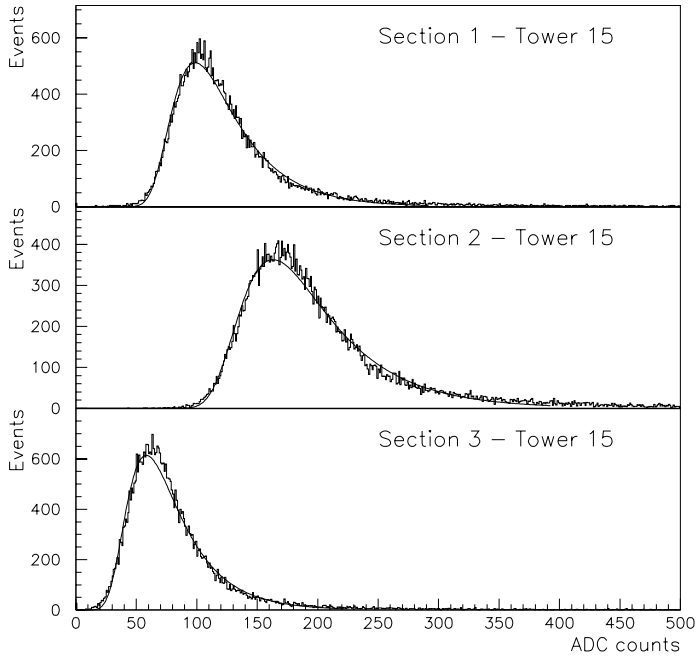

Fig. 15. Typical muon pulse heights for section 1, 2 and 3 towers.

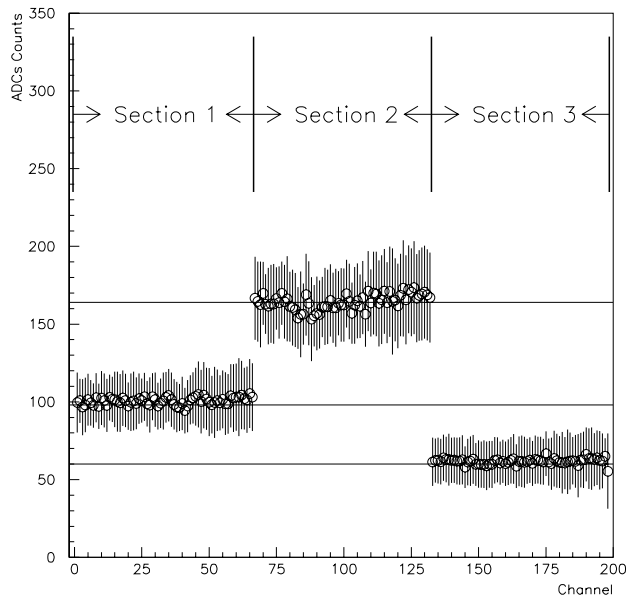

Fig. 16. Result of the gain balancing performed with a muon beam.

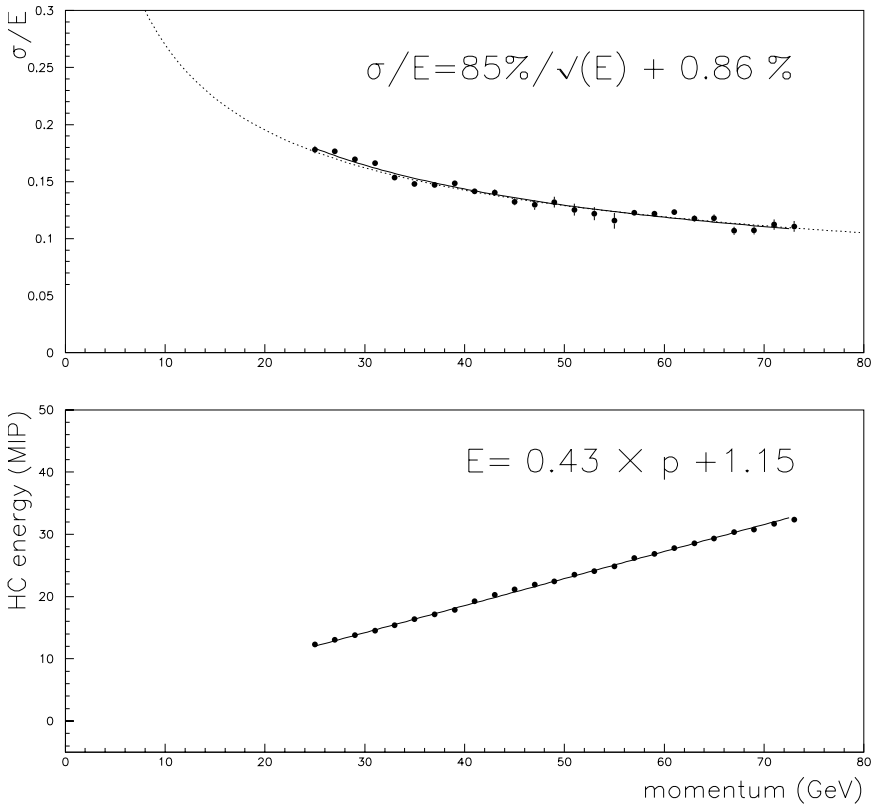

Fig. 17. Pion calibration results: resolution and linearity curves. Solid lines are fit to data, dotted lines are MC simulation.

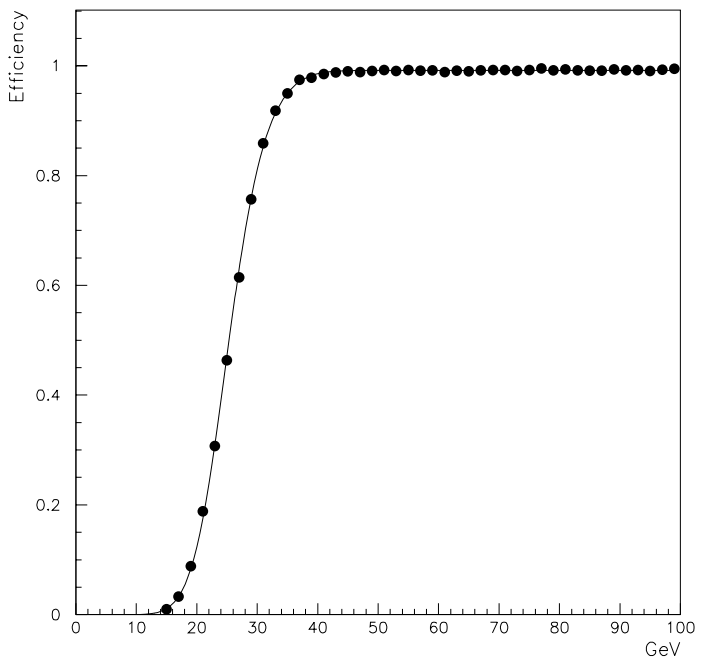

Fig. 18. First lever trigger efficiency versus the total HC energy.